

Research Paper

Nanosonosensitizers for Highly Efficient Sonodynamic Cancer Theranostics

Ju Huang¹, Fengqiu Liu¹, Xiaoxia Han¹, Liang Zhang¹, Zhongqian Hu², Qinqin Jiang¹, Zhigang Wang¹, Haitao Ran¹, Dong Wang³, Pan Li¹✉

1. Institute of Ultrasound Imaging, The Second Affiliated Hospital of Chongqing Medical University, Chongqing 400010, P. R. China;
2. Department of Ultrasound, Zhongda Hospital, Southeast University, Nanjing 210009, P. R. China;
3. Department of Ultrasound, The First Affiliated Hospital of Chongqing Medical University Chongqing 400010, P. R. China.

✉ Corresponding author: Dr. Li (cqclipan@163.com)

© Ivyspring International Publisher. This is an open access article distributed under the terms of the Creative Commons Attribution (CC BY-NC) license (<https://creativecommons.org/licenses/by-nc/4.0/>). See <http://ivyspring.com/terms> for full terms and conditions.

Received: 2018.08.29; Accepted: 2018.10.02; Published: 2018.11.29

Abstract

Background: Multifunctional nanoplatforms with diagnostic-imaging and targeted therapeutic functionality (theranostics) are of great interest in the field of precision nanomedicine. The emerging sonodynamic therapy (SDT) combined with sonosensitizers under the guidance of photoacoustic (PA) imaging is highly expected to accurately eliminate cancer cells/tissue.

Methods: Unique core/shell-structured theranostic FA-HMME-MNPs-PLGA nanoparticles (FHMP NPs, FA: folate, HMME: hematoporphyrin monomethyl ether, MNPs: melanin nanoparticles, PLGA: poly (lactic-co-glycolic) acid) were constructed by the integration of MNPs (for PA imaging) in the core and HMME in the shell for enhanced PA imaging-guided SDT, which were further functionalized with a tumor-targeting ligand, FA. The PA imaging-guided SDT was systematically and successfully demonstrated both *in vitro* and *in vivo*. The high biosafety of FHMP NPs was also systematically evaluated.

Results: The synthesized FHMP NPs with a broad optical absorption not only possess high PA-imaging contrast enhancement capability but also exhibit significant SDT efficiency. Importantly, such a PLGA based nanoplatform improved light stability of HMME, enhancing sonodynamic performance and facilitated delivery of MNPs to the tumor region. Meanwhile, a combined effect between HMME and MNPs was discovered and verified. Furthermore, a sonosensitizer assisted by ultrasound irradiation engenders reactive oxygen species (ROS)-mediated cytotoxicity toward tumor cells/tissue. Both *in vitro* cell-level and systematic *in vivo* xenograft evaluations on tumor-bearing mice demonstrated that the selective killing effect of ROS on tumor cells was assisted by FHMP NPs, which played an active role in the suppression of tumor growth with high biosafety.

Conclusion: A theranostic nanoplatform was successfully constructed, achieving PA imaging-guided SDT against breast cancer cells/tissue. More importantly, MNPs and HMME in one platform with combined effect for enhancing PA imaging was demonstrated. This unique theranostic nanoplatform with multiple capabilities paves a new way toward personalized medicine by rational utilization.

Key words: Nanosonosensitizers, Sonodynamic therapy, Photoacoustic imaging, Melanin, HMME, Nanomedicine

Introduction

As cancer has become one of the most serious threats to human health, the development of new efficient therapeutic modality against cancer has recently attracted tremendous attention. Although traditional therapies, including surgery, chemotherapy and radiotherapy, have been

extensively used and demonstrated to be effective in the treatment of tumors, a variety of ineluctable side effects, including immune system destruction, high cost and low therapeutic efficiency, usually cause the failure of cancer therapy [1, 2]. Therefore, the exploring of the desirable noninvasive and safe

modality for cancer therapy is highly expected. These novel therapeutic modalities should satisfy the strict requirements of targeting/killing cancer cells while keeping the normal cells/tissue undamaged, which is generally accepted as the prospective alternative therapeutic design to traditional cancer-treatment protocols [3].

As one of the emerging therapeutic modality, sonodynamic therapy (SDT) is featured with non-invasiveness, sufficient tissue-penetrating depth, high therapeutic efficiency and mitigated side effects, providing the paradigm of ultrasound (US)-based cancer-therapeutic modality. The therapeutic mechanism of SDT generally involves the cavitation effect of US, which can emit the sono-luminescence to activate the sonosensitizers to produce highly toxic reactive oxygen species (ROS) such as singlet oxygen and hydroxyl radicals [4, 5]. The sonosensitizer-enabled SDT effect has been demonstrated to efficiently induce the apoptosis and death of cancer cells [6-9]. Especially and importantly, versatile cancer types have been reported to be efficiently treated by SDT because of its intrinsically noninvasive feature and high tumor-therapeutic specificity/selectivity [10]. It is noted that SDT has gradually emerged as the desirable option to the mostly explored photodynamic therapy (PDT) for cancer treatment based on the following considerations. First, the light as the irradiation source for PDT suffers from the low tissue-penetrating depth, which can be only effective for the treatment of superficial tumors [11-13]. Second, the cancer patients must be shielded from sunlight after the injection of the photosensitizer to avoid the possible photo-toxicity during the therapeutic procedure [3]. Last but not least, US is a widely accepted, cost-effective and safe clinical imaging modality, which can be easily developed for US imaging-guided therapy with therapeutic guidance and monitoring functionality [12-14]. These unique features make SDT a highly promising noninvasive treatment modality for efficient cancer therapy [13-16].

In general, with the fast development of diagnostic-image technology, molecular imaging has become a new tool for precise diagnosis with high resolution and sensitivity [17]. The construction of multifunctional agents with the integrated functionality of tumor targeting, imaging and therapeutics is of high significance for precision oncology [18, 19]. Photoacoustic (PA) imaging, which converts photon energy into acoustic pressure waves to acquire images, has emerged as a new and nonionizing imaging modality, which provides deep tissue penetration as compared to optical imaging due to the minimized scattering of acoustic waves relative

to light. Accordingly, the design and fabrication of a therapeutic agent to realize PA imaging-guided SDT and simultaneously enhance the efficacy, safety, and accuracy of cancer treatment is of much concern.

Herein, we report, for the first time, on the rational design and construction of a multifunctional theranostic nanoparticles (NPs) with high biosafety for efficient tumor therapy, which has been systematically assessed and demonstrated by both *in vitro* and *in vivo* experiments. Hematoporphyrin monomethyl ether (HMME), a porphyrin-derived sonosensitizer, has a higher tumor-selective uptake by cancer cells than other porphyrin-related agents, as well as the corresponding more pronounced cytotoxic effect when combined with ultrasonic irradiation [20]. Especially, HMME has been extensively used in the diagnosis and treatment of various tumors, including lung cancer, bladder cancer, nevus flammeus and brain glioma [18, 21]. Nonetheless, the intractable problem of its application in clinic is its poor light stability and poor water solubility, leading to the low bioavailability and limited body absorption. Melanin NPs (MNPs), originating from natural biopolymer with excellent biocompatibility and biodegradability, possess broad optical absorption, which makes it a desirable contrast agent for PA imaging [22-25]. Very recently, different types of MNP-based imaging probes have been fabricated, including PEGylated polydopamine NPs (PEG-MNP) [26], PEGylated polydopamine NPs decorated with citraconic amide (PEG-MNP-CA) [27], and PEGylated polydopamine NPs loaded with Gd^{3+} and $^{64}Cu^{2+}$ ($Gd-^{64}Cu$ -PEG-MNP) [2]. Nevertheless, these MNPs suffer from the critical issue of quickly heat diffusion upon PA laser irradiation and poor water solubility, which severely hinders their further broad biomedical application in cancer treatment. On this ground, we utilized poly (lactic-co-glycolic) acid (PLGA), which is a well-known biodegradable and biocompatible polymer approved by the U. S. Food and Drug Administration (FDA) [28], as the vehicle for the co-delivery of therapeutic drugs and functional NPs. The introduction of PLGA to encapsulate MNPs and HMME could not only improve the biocompatibility of HMME but also prevent rapid dissipation of thermal expansion as induced by laser irradiation of MNPs. To overcome the barrier of poor tumor-tissue penetration of the NPs [29], folate (FA) receptor, which is highly overexpressed on the surface of a spectrum of solid tumor cells, has been extensively used as the targeted entity with specific tumor cells/tissue selectivity [30]. Taken together, herein, we developed FA receptor-targeted multifunctional NPs with a combination of MNPs and HMME for achieving intriguing tumor-targeted and PA

imaging-guided SDT against cancer. In this nanosystem, MNPs acted as the PA-imaging contrast agent, while HMME served as the sonosensitizer for enhanced SDT. It has been demonstrated that MNPs could bind to aromatic drugs *via* π - π interaction [22] and porphyrin possessed an aromatic structure, which is a highly conjugated system [31]. Therefore, it is highly expected that the co-encapsulation of MNPs and HMME in one platform could generate a combined effect. Intriguingly, it has been discovered that the MNPs substantially increased the encapsulation efficiency of HMME and further produced synergetic effect on contrast-enhanced PA imaging *in vitro*. After being injected into the mouse *via* tail vein, the FA-HMME-MNPs-PLGA NPs (designed as "FHMP NPs") efficiently accumulated into the tumor tissue through active FA targeting. Subsequently, the systematic *in vitro* and *in vivo* evaluation demonstrated that under the guidance of PA imaging, these multifunctional NPs for SDT yielded a great amount of ROS by the US activation, which markedly suppressed the tumor growth in a mouse breast cancer model (Figure 1).

Materials and Methods

Materials and reagents

The poly (lactic-co-glycolic) acid (PLGA) (50:50, MW: 12000) was obtained from Daigang BIO Engineer Ltd., Co. (Shan Dong, China). Hematoporphyrin monomethyl ether (HMME) was purchased from Shanghai DB Chemical Technology Ltd., Co. (Shanghai, China). 1,3-Diphenylisobenzofuran (DPBF) was obtained from Shanghai Mclean

Biochemical Science and Technology Ltd., Co. (Shanghai, China). N-acetyl-L-cysteine (NAC) was obtained from Beyotime Biotechnology Ltd., Co. (Shanghai, China). Chloroform (CHCl_3) and isopropyl alcohol were purchased from Chongqing East Chemical Industry Ltd., Co. (Chongqing, China). Melanin NPs (MNPs), poly(vinyl alcohol) (PVA, MW: 25000), free folate (FA), polyethylene glycol (PEG), 2,7-dichlorodihydrofluoresceindiacetate (DCFH-DA), 4,6-diamidino-2-phenylindole (DAPI), 1,1-dioctadecyl-3,3,3',3'-tetramethylindocarbocyanine perchlorate (DiI), 1,1'-dioctadecyl-3,3,3',3'-tetramethylindotricarbocyanine iodide (DiR), Calcein-AM and propidium iodide (PI), free folate (FA) were purchased from Sigma-Aldrich Chemical Co. (St Louis, MO, USA). PEG-PLGA-FA was synthesized by Chongqing Punuo Microbian Technology Ltd., Co. (Chongqing, China). Monoclonal antibodies against folic acid in mice (primary antibody) were obtained from Beijing Hapten and Protein Biomedical Institute (Beijing, China). FITC-labeled anti-mouse IgG antibodies in sheep (second antibody) were purchased from Abcam (USA). Roswell Park Memorial Institute-1640 (RPMI-1640) was purchased from Corning. CCK-8 assay was bought from Dojindo Laboratories (Kumamoto, Japan). Singlet Oxygen Sensor Green (SOSG) was bought from Thermo Fisher Scientific.

Synthesis of FHMP NPs

PEG-PLGA-FA encapsulating HMME and MNPs (termed FHMP NPs) were fabricated *via* a simple double emulsion (water/oil/water: W/O/W) method. First, due to the intrinsically poor water solubility of MNPs, 2 mg MNPs were dissolved in 200 μL of a 0.1 M sodium hydroxide (NaOH) solution and then neutralized with the assistance of sonication to reduce the aggregation of NPs. Next, 2 mg HMME were added into 50 mg PEG-PLGA-FA dissolved in 2 mL trichloromethane (CHCl_3) and then mixed with 200 μL of the MNPs solution (1 mg/mL). Subsequently, the mixture was emulsified using an ultrasonic probe (Sonics & Materials, Inc., USA) at an intensity of 100 W for 3 min (water/oil: W/O). For the second emulsion, 8 mL of a poly (vinyl alcohol) (PVA) solution (w/v = 4%) were added into the above emulsified solution and

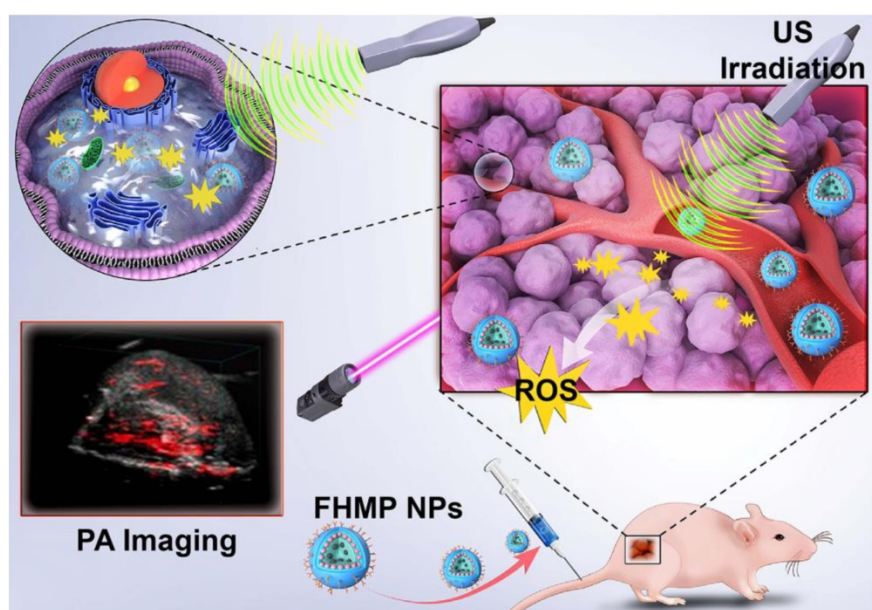


Figure 1. Schematic illustration of the multifunctional nanoplatform for efficiently PA imaging-guided SDT to tumor cells/tissue.

homogenized (FJ300-SH, China) within 2 min. PVA powder was dissolved in distilled deionized water. The as-prepared emulsion was mixed mechanically for 2 h, and CHCl_3 was extracted after adding 10 mL of a 2% isopropyl alcohol solution into the emulsion. Finally, the FHMP NPs were collected after a centrifugation process ($13610 \times g$, 5 min). The pellets were collected for further use. The preparation of HMME-MNPs-PLGA NPs (HMP NPs) was fabricated similar to the above process except that PEG-PLGA-FA was replaced by PEG-PLGA at the same molar ratio. The same method also applied to the synthesis of FA-MNP-PLGA NPs (FMP NPs) and FA-HMME-PLGA NPs (FHP NPs). To prepare fluorescent NPs, DiI or DiR was added to the CHCl_3 solution and covered with silver papers to prevent light exposure, and subsequently, the same procedures were adopted as that detailed above.

Characterization

The morphology and structure of the FHMP NPs were characterized by scanning electron microscopy (SEM, Hitachi S-3400N, Japan) and transmission electron microscopy (TEM, Hitachi H-7600, Japan). The confocal laser scanning microscope (CLSM, A1R; Nikon, Tokyo, Japan) was used to observe the FHMP NPs. The mean particle size and zeta potential were determined using a Malvern Zetasizer Nano ZS instrument (Malvern Instruments, UK). The mean particle sizes of FHMP NPs dissolved in phosphate-buffered solution (PBS) or fetal bovine serum (FBS) were measured with prolonged time duration (1, 2, 3, 4, 5, 6 and 7 days). Then, the differences were observed by the digital photographs. The stabilities of the DiI-FHMP NPs in FBS and PBS were measured by a ultraviolet spectrophotometer (UV-vis: PerkinElmer Lambda 950, USA). The specific method to calculate the encapsulation efficiency was detailed. First, FHMP NPs and HMP NPs were destroyed with CHCl_3 . Then, a certain amount of NaOH solution was added to the mixture for melanin collection. Organic and aqueous phases were separated for HMME and MNPs detection by UV-vis. The encapsulation efficiency was calculated as follows:

$$\text{Encapsulation efficiency (\%)} = \frac{\text{Weight of HMME or MNPs in FHMP/HMP NPs}}{\text{Total weight of HMME or MNPs}} \times 100\%$$

Cell culture

The MDA-MB-231 human breast cancer cell line and A-549 human lung cancer cell line were obtained from Cell Bank of Shanghai Institutes for Biological Sciences (Chinese Academy of Sciences). The cells were cultured in RPMI-1640 medium supplemented

with 10% FBS and 1% penicillin/streptomycin. The cells were maintained in an incubator with a humidified atmosphere containing 5% CO_2 at 37 °C. Cells in a logarithmic growth phase were used for the experiments. When a high attachment efficacy was observed, a 0.25% trypsin-EDTA solution was used to harvest the cells for further use.

In vitro ROS generation from FHMP NPs by US activation

In vitro ROS production following US was measured by DPBF using a UV-vis spectrophotometer. DPBF (2 mL) dissolved in absolute ethanol was added into different nanoparticle solutions. In addition, the mixture was irradiated by low-intensity focused ultrasound instrument (LIFU, LM.SC051 ACA; Institute of Ultrasound Imaging of Chongqing Medical Sciences, Chongqing, China) at an intensity of 1.5 W/cm² and a frequency of 1 MHz for 30 s in the dark. Then, the mixture was extracted three times by CHCl_3 . Finally, the absorbance of DPBF in each group was determined by UV-vis. The DPBF consumption was calculated as follows: DPBF consumption (%) = (the DPBF absorbance before irradiation - the DPBF absorbance post irradiation / the absorbance before irradiation) \times 100%. The SOSG was also applied for detection ROS production. The SOSG solution was added into the FHMP NPs solution (1 mg/mL, 3 mL), and then the mixture was irradiated by the US at different time (0 s, 30 s, 60 s, 90 s and 120 s). To detect the influence of PA laser on the ROS production of FHMP NPs. First, the FHMP NPs were irradiated by PA laser and then they were irradiated by US. The DPBF consumption of FHMP NPs combined with US and FHMP NPs combined with PA laser irradiation and US was compared.

Intracellular ROS production following US was detected using DCFH-DA, a ROS assay kit. MDA-MD-231 cells seeded in culture dishes at a density of 1×10^5 cells per dish were divided into seven groups: control group (Control), US only group (US), FMP NPs combined with US group (FMP NPs + US), FHMP NPs group (FHMP NPs), HMP NPs combined with US group (HMP NPs + US), NAC + FHMP NPs combined with US (NAC + FHMP NPs) and FMHP NPs combined with US (FMHP NPs + US). After 24 h, different treatments were applied to each group. Following coincubation with different NPs (100 μL , 1 mg/mL) for 3 h, the DCFH-DA was added into each dish and incubated for 30 min. Especially, the NAC + FHMP NPs group was treated with NAC. After incubation, the cells were exposed to US irradiation at an intensity of 1.5 W/cm² at a frequency of 1 MHz for 30 s. Half an hour later, the qualitative

analysis of ROS produced by FHMP NPs was detected by CLSM. The corresponding quantitative analysis was obtained after cells were harvested, treated with 0.25% trypsin-EDTA solution, rinsed in PBS, resuspended and determined by flow cytometry (BD FACSVantage SE, USA).

In vitro cytotoxicity assay and in vitro SDT

The cells were seeded in 96-well culture plates at a density of 1×10^4 cells per well in RPMI-1640 medium at 37 °C in the presence of 5% CO₂ for 24 h to allow the cells to adhere to the plates. Then, the above culture medium was replaced with fresh culture medium containing FHMP NPs at different concentrations (0, 2.5, 5, 7.5 and 1 mg/mL). After 3 h, 6 h and 24 h of incubation, the CCK-8 assay was used to evaluate the viability of cells. The optical density (OD) at 450 nm was read with an EL× 800 Universal Microplate Reader (Bio-Tek Instrument Inc., USA). Then, MDA-MB-231 cells were seeded in 96-well plates at a density of 1×10^4 cells per well in RPMI-1640 medium at 37 °C in the presence of 5% CO₂ for 24 h before treatment. These cells were randomly divided into the following groups: the control group (Control), the group subjected to US only (US), the group treated with FMP NPs combined with US (FMP NPs + US), the group treated with FHMP NPs (FHMP NPs), the group treated with HMP NPs combined with US (HMP NPs + US), and the group treated with FHMP NPs combined with US (FHMP NPs + US). The culture medium was removed, and then different NPs (FMP NPs, HMP NPs and FHMP NPs) were dispersed in RPMI-1640 at a concentration of 0.75 mg/mL or 1 mg/mL and added into the wells (100 µL/well). After 3 h of incubation, the dishes with cells were rinsed with PBS three times to remove the unbound NPs. These cells were then treated by LIFU at an intensity of 1.5 W/cm² and a frequency of 1 MHz for 30 s. Finally, a standard CCK-8 assay was used to evaluate the viability of the cells, and the cell viability rate was calculated.

To further exam the effect of SDT for cancer cells, MDA-MB-231 cells were seeded in CLSM-exclusive culture dishes at a density of 1×10^5 cells per well and allowed to adhere overnight. The cells were divided into six groups: the control group (Control), the group subjected to US only (US), FMP NPs combined with US irradiation (FMP NPs + US), FHMP NPs only (FHMP NPs), HMP NPs combined with US irradiation (HMP NPs + US) and FHMP NPs combined with US irradiation (FHMP NPs + US). Then, the cells were incubated with different NPs (FMP NPs, HMP NPs or FHMP NPs) for 3 h. After removing the unbound NPs, the cells were irradiated

by the LIFU at an intensity of 1.5 W/cm² and a frequency of 1 MHz for 30 s. MDA-MB-231 cells were incubated with 0.5 mL Calcein-AM diluted with PBS at a ratio of 1: 1000 and 0.5 mL PI solution diluted with PBS at a ratio of 1: 500 for 15 min. Living cells and dead cells were stained with Calcein-AM (green fluorescence) and PI (red fluorescence) solutions, respectively.

Animal model

All female BALB/c nude mice (6~8 weeks old) were obtained from the Experimental Animal Center of Chongqing Medical University and housed in a suitable environment where they were free to drink water and eat. All experiments were approved by the Institutional Animal Care and Use Committee of Chongqing Medical University. For the establishment of the tumor model, each nude mouse was subcutaneously injected in the right flank with 1×10^6 MDA-MB-231 cells suspended in 100 µL PBS solution.

Targeting ability of FHMP NPs

The structure of FA on the FA-PEG-PLGA was detected by ¹H nuclear magnetic resonance (¹HNMR, Mettler Toledo, Switzerland). Immunofluorescence was applied to assess the immunogenicity of FA on the surface of the FHMP NPs. First, DiI-labeled FHMP NPs and DiI-HMP NPs were fabricated. Then, monoclonal antibodies against folic acid in mice (primary antibodies) were added to the FHMP NPs or HMP NPs emulsion, incubated and washed by PBS. Finally, FITC-labeled anti-mouse IgG antibodies in sheep (secondary antibodies) were coincubated with the above NPs. Following a wash with PBS, the immunogenicity of FA was detected by CLSM and flow cytometry. CLSM-exclusive culture dishes were used to seed MDA-MB-231 cells at a density of 1×10^5 cells per well, and the cells were allowed to adhere overnight. The cells were divided into four groups: control group (Control), HMP NPs group (HMP NPs), free FA + FHMP NPs group (Free FA + FHMP NPs) and FHMP NPs group (FHMP NPs). After 24 h of incubation, the FHMP NPs group was incubated with 200 µL DiI-labeled-FHMP NPs emulsions (1 mg/mL). The HMP NPs group was supplemented with 200 µL DiI-labeled HMP NPs emulsions (1 mg/mL). The free FA + FHMP NPs group was incubated with free FA (1 mol/L, 1 mL) for 1 h and then mixed with 200 µL DiI-labeled FHMP NPs emulsions (1 mg/mL). After a 3 h coincubation with nanoemulsions, the cells in all groups were washed with PBS three times, fixed with 4% paraformaldehyde (1 mL) for 15 min, and incubated with DAPI (200 µL) for 15 min. Finally, the fluorescence images of the treated cells were acquired by CLSM. To exam the specific targeting of FHMP

NPs to MDA-MB-231 cells, the A549 cell line was applied as the control group. MDA-MB-231 and A549 cells were incubated with FHMP NPs for 3 h. Next, CLSM was used to observe the ability of FHMP NPs to target different cells.

Nine MDA-MB-231 tumor-bearing mice were divided into three groups ($n = 3$ each group): HMP NPs, Free FA + FHMP NPs and FHMP NPs. First, the mice in group of Free FA + FHMP NPs were administrated with free FA solution. Then, after injection of FHMP NPs or HMP NPs (200 μL , 10 mg/mL), the fluorescence images were acquired at various times post injection (0 h, 0.5 h, 2 h, 4 h, 6 h and 24 h) by using a fluorescence system (F7 Ir Spectra, Vilber Lourmat, France) with excitation and emission wavelengths of 748 nm and 780 nm, respectively. Then, major organs of the mice were collected for fluorescence imaging. The corresponding fluorescence signal was calculated by the fluorescence analysis system. In addition, the mice received the same treatment as those described above except that the nanoemulsions were labeled with DiI. At 2, 4, and 24 h post injection, tumors were immediately dissected for ultrathin sections and then the sections were stained with DAPI for fluorescence microscopy detection.

In vitro and in vivo PA imaging

For *in vitro* PA imaging, different concentrations of FHMP NPs and HMP NPs (5, 10, 15, 20 and 25 mg/mL) dissolved in water were used for PA signal detection and to evaluate the linearity of the PA signal as a function of FHMP NPs concentration. The PA values of the FHMP NPs, FMP NPs and FHMP NPs at concentrations of 5 mg/mL, 17.5 mg/mL, 30 mg/mL, respectively, were recorded *in vitro*. The PA images of the unencapsulated MNPs and FMP NPs were also calculated *in vitro*. The PA images were obtained by the VEVO LASR PA imaging system (VIVO 2100; FUJIFILM Visual Sonics, Inc., Canada). For *in vivo* PA imaging, the images were observed using MDA-MB-231 tumor-bearing mice, which were divided into three groups (HMP NPs, Free FA + HMP NPs and FHMP NPs) ($n = 3$). After intravenously injecting 200 μL (10 mg/mL) HMP NPs or FHMP NPs emulsions at different time points (0 h, 1 h, 2 h, 4 h, 6 h and 24 h), the corresponding PA images were simultaneously recorded by the VEVO LASER PA imaging system. Especially, the mice in group of Free FA + FHMP NPs were injected with free FA solution before the administration of FHMP NPs.

In vivo SDT of FHMP NPs

When the tumor volume reached 0.8 cm^3 , the mice were randomly assigned to five groups (Control,

US, FMP NPs + US, FHMP NPs, FHMP NPs + US). After intravenous injection of 200 μL (10 mg/mL) different NPs for 3 h, the regions of the tumors were irradiated by US (3 W/ cm^2 , 1 MHz) for 5 min. The treatment was repeated every three days. Tumor volumes and body weights of the mice were recorded every three days. Tumors were dissected after the treatment ended, and the weights were recorded; the tumors were then fixed with 4% polyoxymethylene for histological analysis including H&E, TUNEL and PCNA (H&E: hematoxylin-eosin staining; TUNEL: TdT-mediated dUTP nick-end labeling; PCNA: proliferating cell nuclear antigen). According to the weight of the tumors, the tumor inhibition rate was determined.

In vivo toxicity

Twenty-four female nude mice were divided into two groups (Control and FHMP NPs). The FHMP NPs emulsions (200 μL , 10 mg/mL) were intravenously injected into the mice. The mice were sacrificed at various time points after injection (1 h, 6 h, 24 h and 48 h), and 0.8 mL blood was collected for blood panel analysis and biochemistry assay. The major organs of the mice (liver, spleen, kidney, heart and lung) were harvested and fixed with 4% polyoxymethylene for H&E staining.

Statistical analysis

All statistical analyses were performed with SPSS 20.0 software. Data were presented as the mean \pm standard deviation. The significance of the data was analyzed according to the Student's *t* test: * $P < 0.05$, ** $P < 0.01$.

Results and discussion

Synthesis and characterization of FHMP NPs

The constructed multifunctional FHMP NPs were synthesized following the strategy as shown in **Figure 2A**. We obtained the FHMP NPs *via* a double-emulsion approach [32-35], which was expertly mastered [32, 36-38]. First, the obtained FHMP NPs displayed a well-defined spherical shape and homogenous size, as revealed by SEM (**Figure 2B**) and TEM images (**Figure 2C** and **Figure S1A**). In addition, the FHMP NPs exhibited strong red fluorescence, as detected by CLSM (**Figure 2D**), which matched well with the SEM and TEM results. The mean diameters of the FHMP NPs, FHP NPs and FMP NPs were 310.3 ± 10.6 nm (**Figure 2E**), 266.1 ± 2.4 nm (**Figure S1B**) and 270.1 ± 4.9 nm (**Figure S1C**), respectively, showing a relatively narrow size distribution and no significant difference among them. The size of PLGA nanoparticles could be managed by setting up parameters of sonication (e.g.,

power, interval) or adjusting polymer concentration in organic phase, which has been demonstrated [39]. However, the relatively large particle size guarantee the high encapsulation efficiencies of MNPs and HMME in the FHMP NPs. In addition, the average zeta potentials of FHP NPs, FMP NPs and FHMP NPs were -21.4 ± 1.7 mV, -21.2 ± 0.8 mV and -23.03 ± 1.33 mV (**Figure S1D**), respectively. Meanwhile, the mean particle size of FHMP NPs did not show appreciable change when dissolved in PBS or FBS, and the particle suspension did not aggregate or precipitate within 7 days, revealing the excellent long-term stability of the FHMP NPs (**Figure 2F and Figure S1E**). Next, the stability of DiI-FHMPs in PBS and FBS 48 h later was further investigated by determining the dye content in the supernatant of DiI-labeled FHMP NPs *via* UV-vis spectrophotometry. As shown in **Figure 2G**, there was

no detectable free DiI dye in the solution, indicating that FHMP NPs were highly stable in both PBS and FBS. **Figure S1F, S1G, S1H and S1I** present the relative absorbances of the HMME and MNP solutions, respectively, revealing a desirable linear relationship between optical density and concentration. The encapsulation efficiencies of HMME and MNPs in FHMP NPs were $80.13 \pm 4.81\%$ and $47.72 \pm 4.26\%$, respectively. In addition, the encapsulation efficiencies of HMME and MNPs in HMP NPs were $79.13 \pm 81\%$ and $44.72 \pm 3.25\%$, respectively. The encapsulation efficiencies of HMME or MNPs in FHMP NPs and HMP NPs did not show a significant change, indicating that attachment of FA to PEG-PLGA had no obvious effect on the encapsulations of the guest molecules.

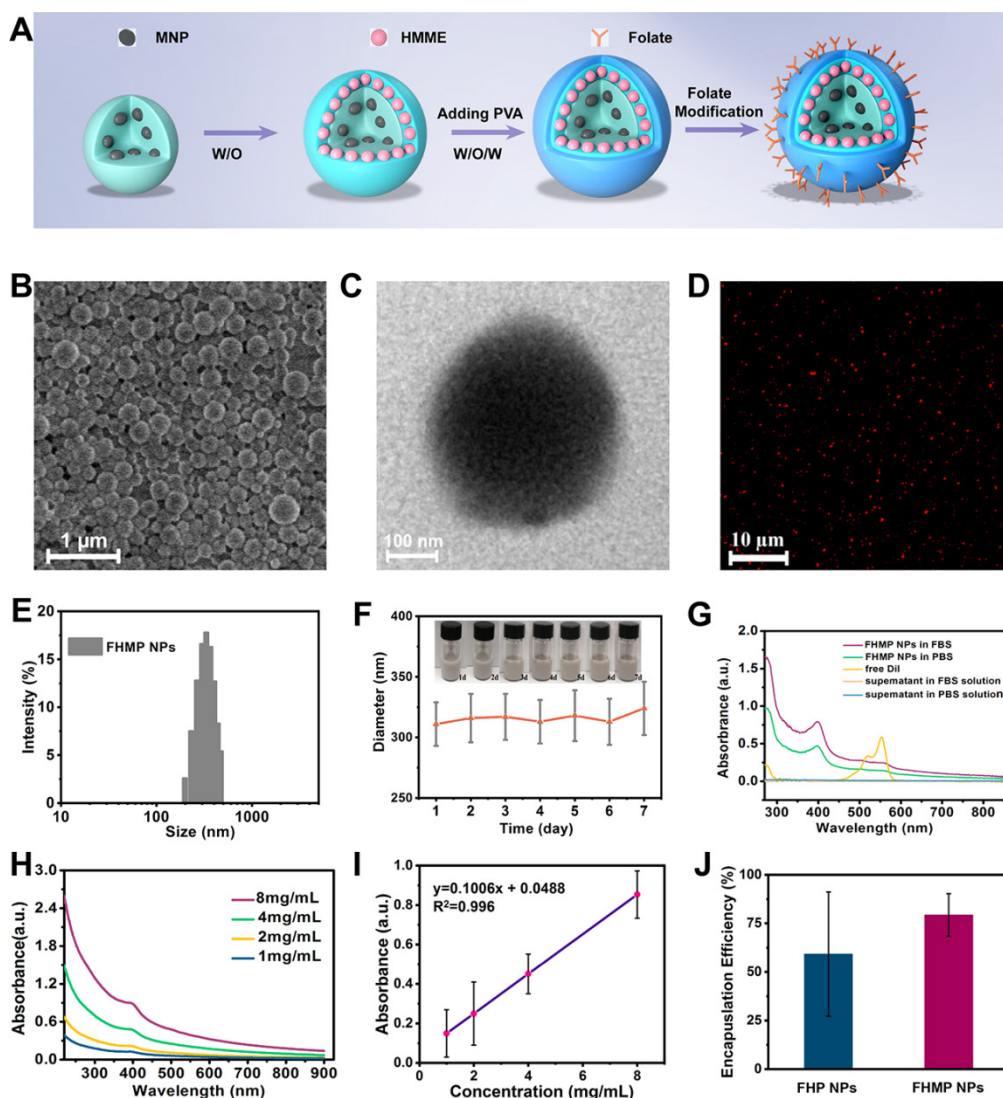


Figure 2. Morphology and characterization. **(A)** Schematic diagram for the fabrication of FHMP NPs. **(B)** SEM and **(C)** TEM of FHMP NPs. **(D)** CLSM image of DiI-stained FHMP NPs. **(E)** Size distribution of FHMP NPs and **(F)** The size distribution with prolonged time duration. Inset: digital photos of the FHMP NPs dispersed in PBS (25 mg/mL). **(G)** UV-vis absorbance of free DiI dye labelled FHMP NPs in FBS and PBS, the corresponding supernatant solutions after 24 h incubation. **(H)** UV-spectra of FHMP NPs dispersed in aqueous solution in different concentrations (1, 2, 4 and 8 mg/mL) and **(I)** corresponding relationship between concentration of FHMP NPs and absorbance ($n = 3$). **(J)** The encapsulation efficiency of HMME in FHP NPs and FHMP NPs ($n = 3$).

In addition, the absorption wavelength of the obtained FHMP NPs (Figure 2H) covered a wide range in the UV visible region, with a good linear relationship between optical density and concentration (Figure 2I). On the basis of the binding capability of MNPs to aromatic drugs, it is hypothesized that the combination of MNPs and HMME could increase the encapsulation efficiency of HMME in the NPs. As shown in Figure 2J, the encapsulation efficiency of HMME in FHMP NPs was significantly improved compared to that in FHP NPs.

In vitro toxicity and SDT of cancer cells

The level of ROS production is essential for SDT [40]. Given that HMME is one of the promising forms of sonosensitizers, in this study, DPBF was applied to

detect the production of ROS. As the absorbance intensity of DPBF at 410 nm in the UV-vis spectrum decreases when oxidized by $^1\text{O}_2$ [41], the DPBF consumption helps to calculate the ROS production. According to Figure 3A, the relative DPBF consumption in the group of FHMP NPs plus US was notably higher compared to those in other control groups. Otherwise, as the typical sensor, SOSG was used to determine $^1\text{O}_2$ production after ultrasound irradiation for different time duration. According to Figure S2A, with prolonged irradiation time, the FHMP NPs exhibited obvious higher ROS production efficacy, indicating their potential as sonosensitizer for SDT.

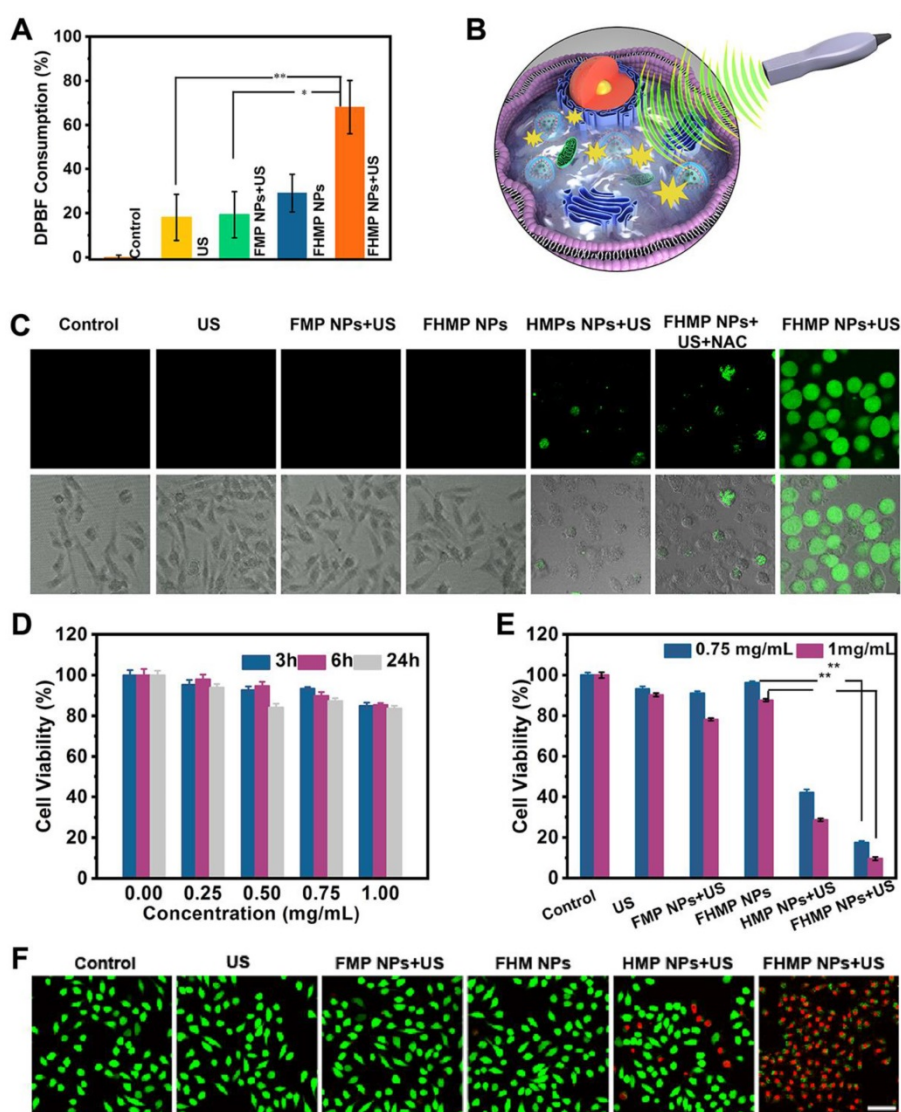


Figure 3. In vitro SDT of cancer cells. (A) Relative DPBF consumption of different nanoparticles under different treatments. ($n = 3$, $*p < 0.05$ and $**p < 0.01$). (B) The scheme of FHMP NPs as a sonosensitizer for cancer therapy. (C) Intracellular ROS generation capacity illustrated by CLSM images of MDA-MB-231 cells. The scale bar is 10 μm . (D) Relative cell viability of MDA-MB-231 cells after incubation with various concentrations (0, 0.25, 0.5, 0.75 and 1 mg/mL) of FHMP NPs for 3 h, 6 h and 24 h ($n = 3$) (E) Relative cell viability of MDA-MB 231 cells after different treatments including Control (without treatment), US, FMP NPs combined with US irradiation, FHMP NPs only, HMP NPs combined with US irradiation, and FHMP NPs combined with US irradiation ($n = 3$). (F) CLSM images of MDA-MB-231 cells after different treatments. The scale bar is 20 μm .

As a sonosensitizer compound, the photostability of FHMP NPs in the platform plays a crucial role in initiating ROS for their *in vivo* application. Hence, we determined the relative DPBF consumption, which represents ROS production, to assess the stability of FHMP NPs upon PA laser exposure. DPBF consumption in FHMP NPs + PA laser + US group has been performed (**Figure S2B**) and it has been found there was no significant difference compare to the FHMP NPs + US group, indicating FHMP NPs remained a good photostability under PA laser and could be highly activated by US.

Next, the *in vitro* toxicity and SDT effectiveness of FHMP NPs on MDA-MB-231 cells were explored (**Figure 3B**). First, we investigated the potential of FHMP NPs to produce intracellular ROS under US stimulation using DCFH-DA as a ROS molecular probe. DCFH-DA itself has no fluorescence but can be converted into fluorescent 2', 7'-dichlorofluorescein (DCF) after reacting with ROS [42]; therefore, it can be used to assess ROS generation. To detect and quantify the production of ROS, we hereby determined the fluorescence signal from DCF with CLSM and flow cytometry. The CLSM images from **Figure 3C** present strong green fluorescence in the group of FHMP NPs plus US exposure, revealing the mass production of ROS from FHMP NPs in tumor cells after US activation. In contrast, no evident fluorescence signal was displayed in the remaining groups, including control (without treatment), US, FMP NPs + US, FHMP NPs and HMP NPs +US. In particular, when NAC, known as an ROS scavenger [43], was added to the group of FHMP NPs + US, ROS generation was vastly impeded; thus, a lower fluorescence intensity was observed under these circumstances. The fluorescence intensity after the above treatments was further quantified using flow cytometry, as shown in **Figure S3 and S4**. The relative fluorescence intensity in the treated group with FHMP NPs +US was significantly higher than that in any other group, which is well consistent with the CLSM observation in **Figure 3C**.

Then, the cells were incubated with these NPs at various concentrations (0, 0.25, 0.50, 0.75 and 1.00 mg/mL) for 3, 6 and 24 h, and then the *in vitro* toxicity to cells was tested using a standard CCK-8 assay. As shown in **Figure 3D**, FHMP NPs only exerted a negligible effect on the survival of MDA-MD-231 cells without US activation even at concentration up to 1.00 mg/mL, indicating their favorable biocompatibility for further utilization.

To verify the SDT effectiveness of FHMP NPs, the cells were then incubated with various types of NPs (FMP NPs, HMP NPs, and FHMP NPs) for 3 h at the concentrations of 0.75 mg/mL and 1.00 mg/mL,

either followed by US irradiation or not irradiated. Strikingly, it was found that the US-activated HMP NPs and FHMP NPs generated a strong cytotoxicity effect on MDA-MD-231 cells, and the FHMP NPs caused the lowest cell viability (**Figure 3E**), while no evident decline was observed after the cells were treated with FHMP NPs alone without US irradiation, revealing that the targeted nanosonosensitizers under US activation mainly contributed to the cell-killing effect. This efficacy of targeted SDT was further confirmed by a Calcein-AM and PI co-staining test for differentiating live cells from dead cells. Likewise, highest numbers of dead cells were found under CLSM after FHMP NPs were combined with US treatment (**Figure 3F**). No significant effect on cell viability was shown after treatment with US, FMP or FHMP NPs. These results demonstrated that FHMP NPs had high biocompatibility. However, in the meantime, they also acted as an efficient sonosensitizer to produce the targeted SDT effect on cancer cells when activated by US.

Targeting ability of FHMP NPs

The structure of shell materials of FHMP NPs formed from FA-PEG-PLGA was confirmed by ¹HNMR spectroscopy, as shown in **Figure 4A**, proving the efficient connection of FA and PEG to PLGA. Then, immunofluorescence was applied to assess the immunogenicity of FA on the surface of the FHMP NPs. CLSM images show that the DiI-labeled NPs present red fluorescence and the FITC-labeled anti-mouse IgG antibodies in sheep (secondary antibodies) exhibit green fluorescence. When the channels were combined, a yellow fluorescence was detected owing to the overlap of red and green fluorescence (**Figure 4B**). The binding efficiency between FA and HMP NPs was $94.37 \pm 6.59\%$, as determined by flow cytometry (**Figure 4C**). In addition, the efficacy of DiI-labeled FHMP NPs to target MDA-MB-231 cells was verified by the CLSM. As shown in **Figure 4D**, numerous DiI-labeled FHMP NPs emitted red fluorescence and aggregated around the cells after 3 h of coincubation. Meanwhile, only a few NPs gathered around the cells in the other two groups (HMP NPs and Free FA + FHMP NPs). To demonstrate the role of FA in guiding FHMP NPs to FA receptor-rich tumor cells, the FHMP NPs were also incubated with FA receptor-negative A549 lung carcinoma cells [44-46] as control for 1 h, 2 h and 3 h. Compared to that in MDA-MB-231 cells, the fluorescence signal visible in A-549 cells was very weak even after being incubated for 3 h (**Figure 4E**). The marked difference between these two cell lines suggests that the FHMP NPs specifically targeted toward FA receptor-rich tumor cells.

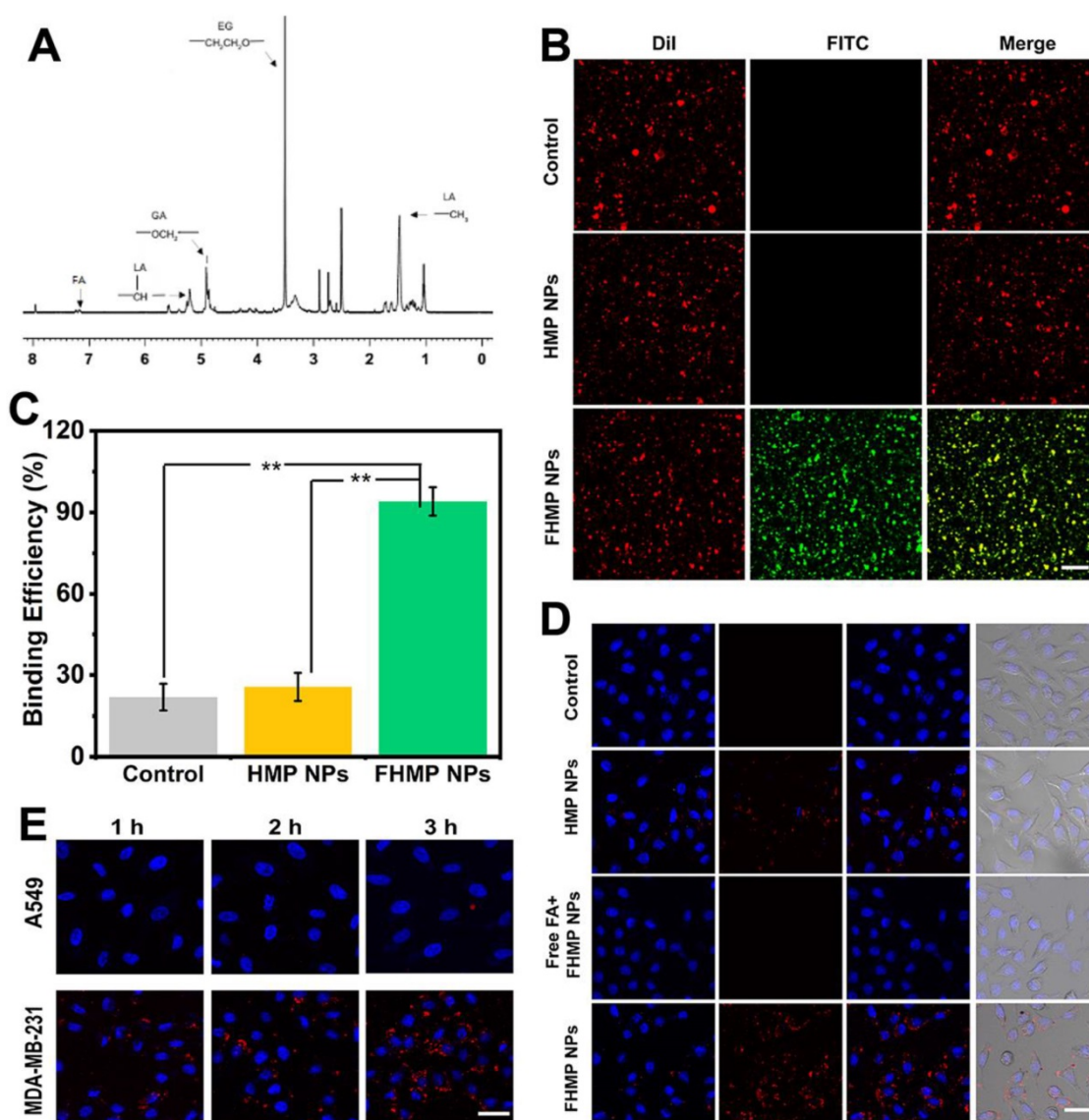


Figure 4. (A) The ^1H NMR spectrum of FA-PEG-PLGA. (B) The investigation of FA on the surface of NPs by CLSM. The scale bar is 10 μm . (C) The binding efficiencies of different NPs detected by flow cytometry ($n = 3$, $**p < 0.01$). (D) CLSM images of MDA-MB-231 cells after incubation with different NPs. (Dil-labeled-HMP NPs, free folic acid (FA) combined with Dil-labeled FHMP NPs and Dil-labeled FHMP NPs) for 3 h. The scale bar is 20 μm . (E) CLSM images of MDA-MB-231 cells and A-549 cells after incubation with Dil-labeled FHMP NPs for elevated time (1 h, 2 h and 3 h). The scale bar is 15 μm .

To further validate the active targeting efficiency *in vivo*, the MDA-MB-231 tumor-bearing mouse model was established, and fluorescence imaging was performed at different time points after tail vein injection with DiR-labeled FHMP NPs or HMP NPs. According to **Figure 5A**, a strong fluorescence signal was observed in the tumor region after injection of DiR-dyed FHMP NPs, while only a faint signal was found in the parallel tumor in mice treated with HMP NPs without FA targeting. Especially, the FA guidance effect was impeded when the mice were injected with free FA, so there were no significant fluorescent signal can be detected even the FHMP NPs administration. Typically, the fluorescence intensity reached a peak value of as high as 8674 (a.u.) at 2 h post-injection through the active targeting of FA

(**Figure 5B**). The average fluorescence intensity in the FHMP NPs group was determined to be 3.6-folds of that in HMP NPs group. To determine the NPs biodistribution *in vivo*, the major organs and tumors were harvested 24 h later for *ex vivo* fluorescence imaging (**Figure 5C**), and the corresponding fluorescence intensities were quantified (**Figure 5D**). In addition, both types of NPs were also found to accumulate in the liver and spleen due to the phagocytosis by the reticuloendothelial system (RES). Examination of ultrathin tumor sections showed that the FHMP NPs group contained many red dots, indicating that the FHMP NPs largely accumulated in the tumor site; the highest number was noted at 2 h. Only a small quantity of red dots was found in tumor sections from the HMP NPs group (**Figure 5E**).

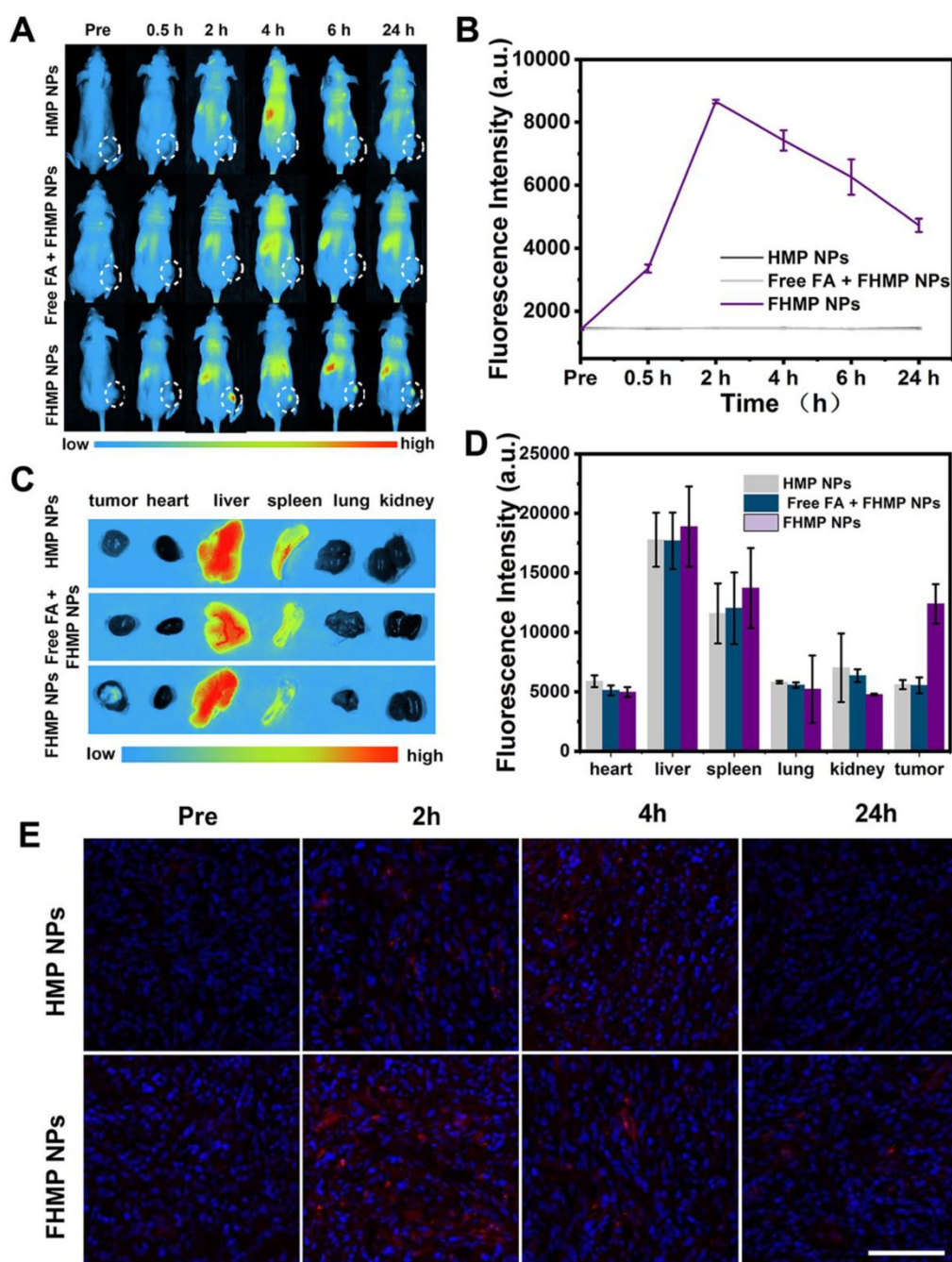


Figure 5. (A) *In vivo* fluorescence imaging and tumor targeting of a mouse at 0.5 h, 2 h, 4 h, 6 h and 24 h postinjection of tumor-bearing mice. (B) Quantitative fluorescence intensity of tumor tissue at different times ($n = 3$). (C) Biodistribution of DiI-labeled FHMP NPs or HMP NPs in major organs excised from mice at 24 h postinjection. (D) Corresponding quantitative analysis of fluorescence intensity in major organs ($n = 3$, $**p < 0.01$). (E) Ultrathin section of tumor tissues at different time points (2 h, 4 h and 24 h) post-injection of DiI-labeled FHMP NPs or HMP NPs detect by fluorescence microscope. The scale bar is 100 μm .

In vitro and *in vivo* PA imaging

To explore the potential of FHMP NPs as a PA probe for tumor imaging, which is especially helpful in analyzing information in the tumor area, PA imaging was acquired using FHMP NPs as the contrast agent both *in vitro* and *in vivo*. With the excitation wavelength ranging from 700 nm to 950 nm, FHMP NPs had the strongest PA signal at 700 nm (Figure 6A). As shown in Figure 6B, PA images of

HMP NPs and FHMP NPs dispersed in aqueous solution at different concentrations clearly show their contrast-enhancement performances under the excitation at 700 nm. Noteworthy, there were no significant differences between the HMP NPs and FHMP NPs in PA imaging. Under PA laser irradiation, the FMP NPs and MNP (without being encapsulated) solutions at various concentrations were compared for PA imaging *in vitro*, which is shown in Figure S5. Clearly, the FMP NPs emulsions

presented a noticeable PA imaging signal, whereas no significant PA imaging signal was detected in the MNP solution group under the same condition. Based on the fact that MNPs can bind drugs with an aromatic structure, we tested if those two NPs have combined effects in PA imaging. Therefore, we measured the *in vitro* PA values from FHP NPs, FMP NPs and FHMP NPs at the concentrations of 5, 17.5 and 30 mg/mL (Figure 6C, 6D), respectively. It was found that the PA values of FHMP NPs were substantially higher than those of FHP NPs or FMP NPs alone under the same condition, revealing a combined effect on enhancing PA imaging of MNPs and HMME. Motivated by the aforementioned *in vitro* results, *in vivo* PA imaging at tumor sites on the mouse breast cancer model was acquired at different time points after intravenous injection of FHMP NPs or HMP NPs into the mice (Figure 6E), and the

corresponding quantitative analysis of PA values was performed (Figure 6F). Before NPs injection, the tumor showed a negligible PA signal. After injection with FHMP NPs, the PA signal in the tumor region reached maximum value approximately 2 h post-injection. With prolonged time after post-injection, the tumor PA value gradually decreased, which is attributed to the clearance of FHMP NPs from the tumor site. In contrast to the signal from FHMP NPs injection, no obvious PA signal was detected from HMP NPs injection, and the corresponding PA value was also dramatically lower as well the group of free FA + FHMP NPs. These results demonstrate the potential of FHMP NPs as a desirable contrast agent for PA imaging, which leads to diagnostic-imaging guidance and monitoring during tumor therapy.

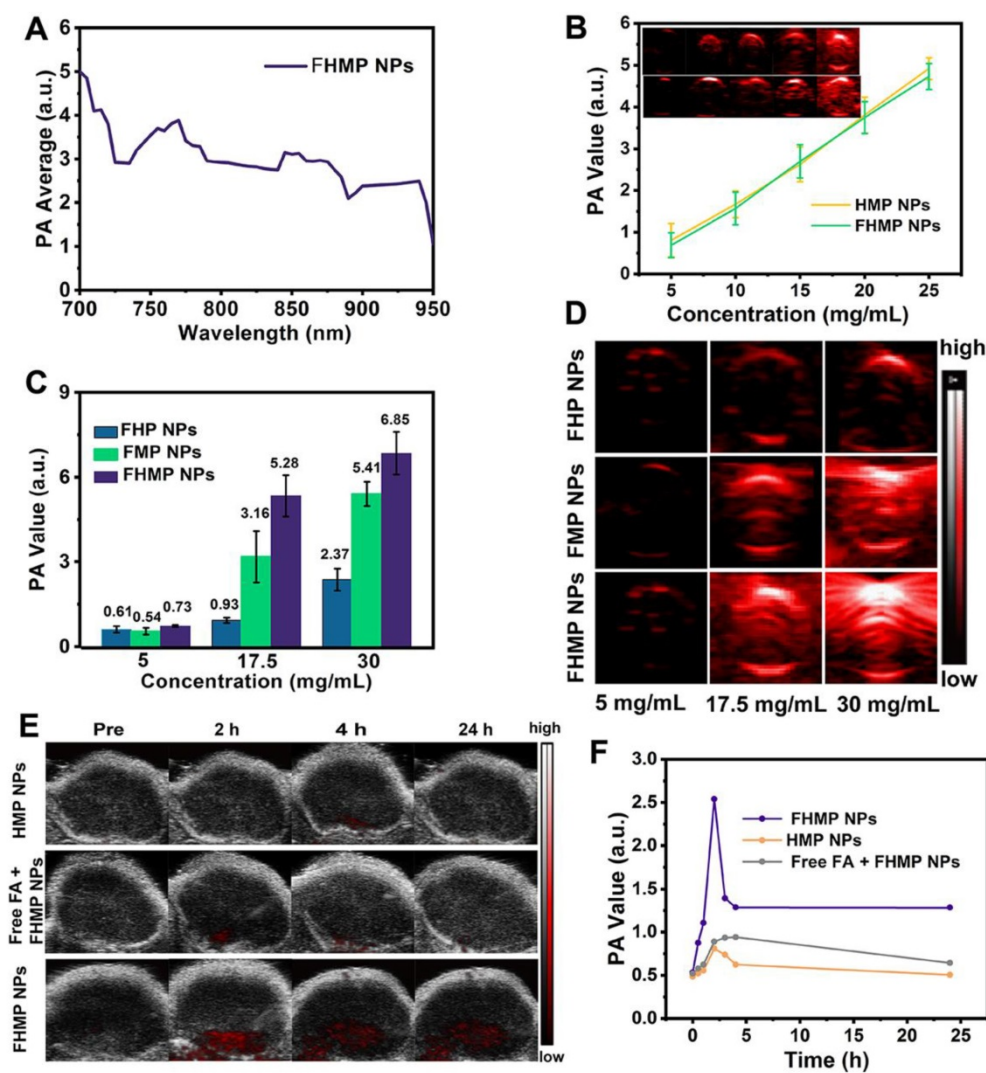


Figure 6. PA imaging of FHMP NPs *in vitro* and *in vivo*. (A) Quantitative PA intensities of FHMP NPs *in vitro*. (B) Plots of PA values of FHMP NPs and HMP NPs with various concentrations of 5, 10, 15, 20 and 25 mg/mL *in vitro*. Inset: PA images of FHMP NPs (the first row) and HMP NPs (the second row) dispersed in aqueous solution ($n = 3$). (C) Quantitative PA values of FHP NPs, FMP NPs and FHMP NPs with different concentrations (5, 17.5 and 30 mg/mL) ($n = 3$) and (D) corresponding PA images of tumor regions in MDA-MB-231-bearing mice after the intravenous injections of HMP NPs or FHMP NPs at varied time intervals (0 h, 2 h, 4 h and 24 h) with 5 mg/mL concentration for 200 μ L of total volume. (E) PA signal at tumor regions in MDA-MB-231-bearing mice.

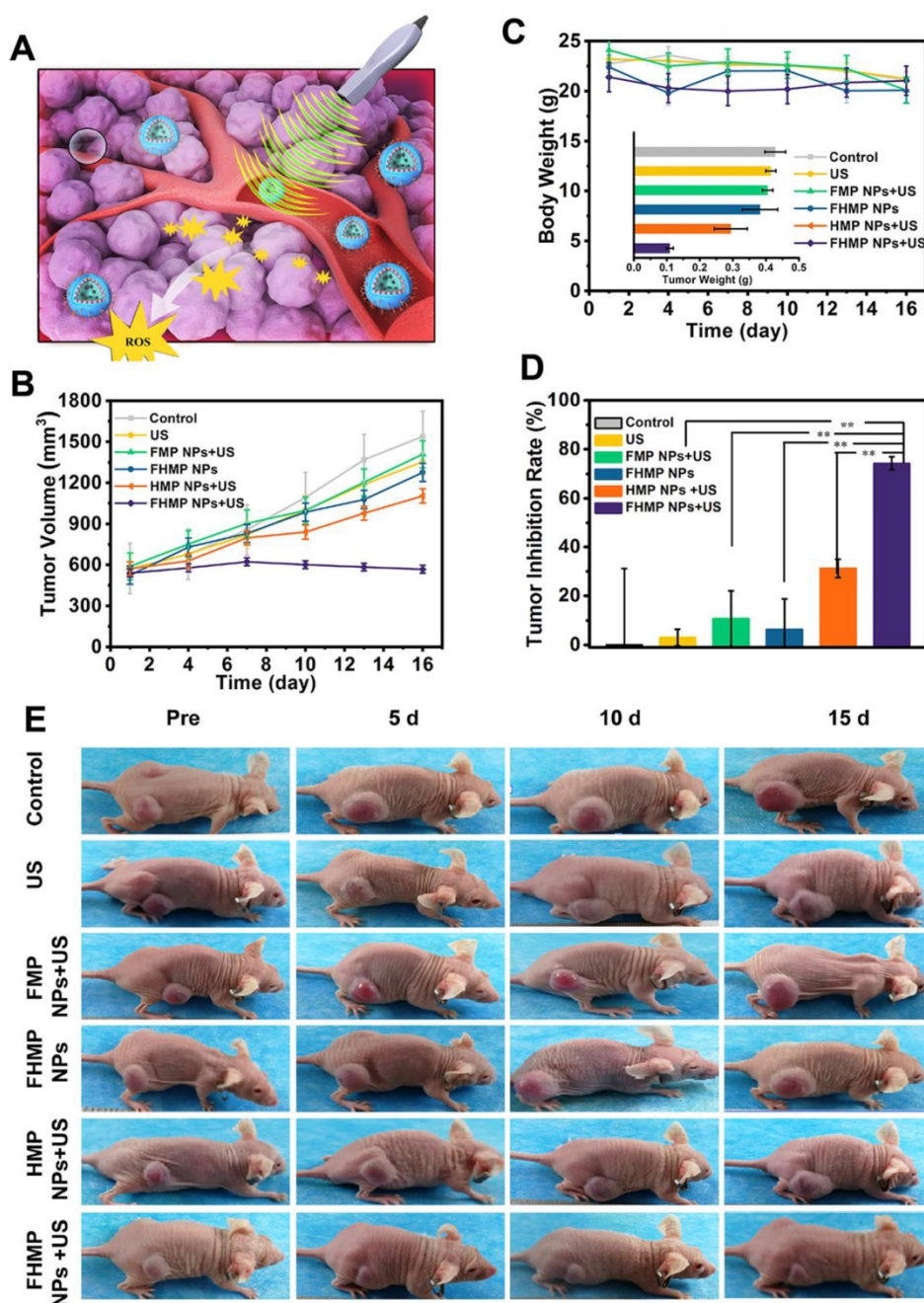


Figure 7. *In vivo* SDT of FHMP NPs. **(A)** Schematic illustration of SDT as assisted by FHMP NPs for cancer cells. **(B)** Time-dependent tumor volume curves (n = 4) and **(C)** Time-dependent body weights of MDA-MB-231-bearing mice in the group of control, US, FMP NPs combined with US, FHMP NPs, HMP NPs combined with US, and FHMP NPs combined with US. Inset: tumor weights of mice after the treatments (n = 4). **(D)** Tumor inhibition rates of MDA-MB-231-bearing mice after different treatments (n = 4, **p < 0.01). **(E)** Photographs of MDA-MB-231 tumor-bearing mice after different treatments in 15 days' period.

In vivo SDT of FHMP NPs

SDT, an effective treatment for malignant tumors, causes minimal damage to adjacent healthy tissues. Encouraged by the excellent PA imaging, ROS generation, and SDT efficiency of FHMP NPs, tumor therapy was performed *in vivo* as depicted in Figure 7A. Six groups (blank control, US control, FMP NPs + US group, FHMP NPs group, HMP NPs + US group and FHMP NPs with US irradiation) were employed to evaluate the SDT efficacy of FHMP NPs. Tumor

volumes and body weights of the mice were monitored every two days, and digital photographs of the mice were taken every five days for fifteen days after the treatment. As shown in Figure 7B, the tumor growth curves displayed that tumor volumes increased rapidly except for the FHMP NPs + US group during the entire treatment period. After fifteen days of treatment, remarkably suppressed tumor growth was observed in the group of FHMP NPs combined with US irradiation, which is ascribed to the effect of SDT on the abundance of ROS generation.

The body weight of the mice showed negligible fluctuations, thus confirming the negligible adverse effects of these treatments on the health of mice (Figure 7C). To further testify the antitumor efficiency of different treatments, tumor weight inhibition rates were calculated after the treatments. From Figure 7D, it can be found that the FHMP NPs + US group exhibited the highest tumor weight inhibition rate compared to any other groups, confirming the efficient tumor suppression by US-activated FHMP NPs. As shown in Figure 7C inside, the weight of the desected tumor masses of various treatments show the similar trend to the Figure 7B. Meanwhile, the digital photographs in Figure 7E show that tumors in the treated group (FHMP NPs + US) were inhibited at the end of the treatment. In comparison, tumors in the remaining groups grew quickly, as no therapeutic efficacy was exerted and there was only a limited inhibitory effect.

In observing H&E and TUNEL staining, substantial damage and apoptosis of tumor cells in

the group of FHMP NPs + US were found, which were much more remarkable compared to those in other control groups (Figure 8A). The highest apoptotic index was also exhibited in this group (Figure 8B). The *in vivo* proliferative activity was determined by PCNA staining, and the group of FHMP NPs + US presented a strong suppression effect on cell proliferation, while the other five groups did not show adverse effects on the proliferative activity of cancer cells (Figure 8C).

In vivo toxicity

It is highly desirable to exploit novel probes that not only have an image-guided therapeutic ability that ensures effective tumor targeting but also possess satisfactory biocompatibility and biodegradability, which ensure their harmless excretion from the body at a specific time after therapy [47]. However, inorganic NPs, such as Au [48], Ag [49], and Pt NPs [50], golden nanostars [51], transition metal sulfide/oxide NPs [52, 53] and carbon nanomaterials

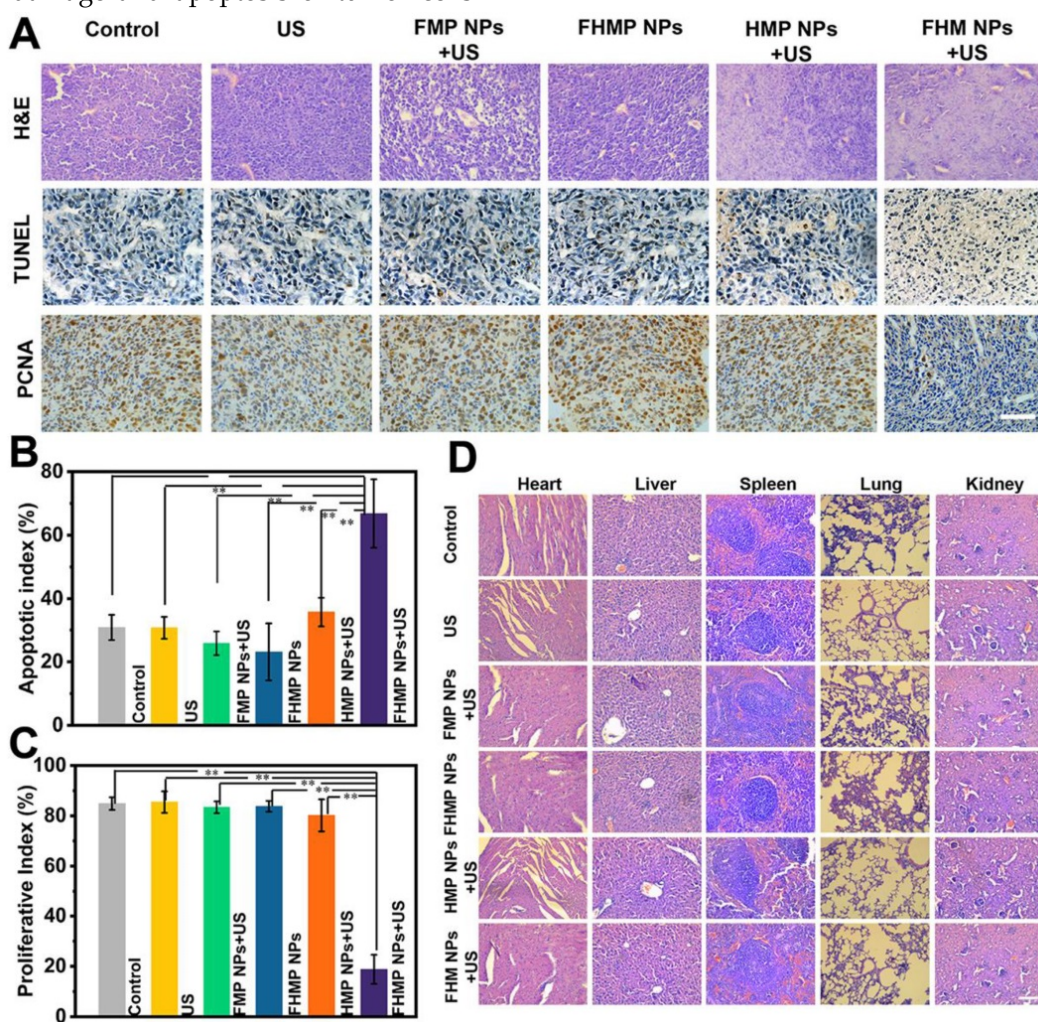


Figure 8. (A) H&E, PCNA and TUNEL staining in tumor region of every group after different treatments. The scale bar is 50 μ m. (B) Quantitative analysis of apoptotic index (n = 4, **p < 0.01) and (C) proliferative index (n = 4, **p < 0.01). (D) H&E staining in major organs (heart, liver, spleen, lung, and kidney) of every group after treatments. Scale bar: 50 μ m.

[54, 55], generally possess poor biodegradability and long-term body retention, causing the risk of adverse effects [56]. The designed FHMP NPs in this study are completely composed of biocompatible and biodegradable ingredients. To prove their potential transition to the clinic, we further conducted a detailed investigation of *in vivo* toxicology. First, the normal hematology parameters, as indicators of many diseases, were examined by observing the blood cells and their morphological distribution. According to **Figure S6A**, compared to that of the control group, changes in the number of blood cells were neglectable, including white blood cells (WBC), red blood cells (RBC) and platelets (PLT), as well as in the morphological distribution of the group of FHMP NPs. Next, the standard blood biochemical indexes were measured, and various makers were tested. In **Figure S6B**, compared with that of the control group, no meaningful change was detected from the indicators of hepatic function, including alanine transaminase (ALT), aspartate transaminase (AST), alkaline phosphatase (ALP) and albumin (ALB), as well as from the renal indicators (urea nitrogen: BUN; and serum creatinine: Scr), in the FHMP NPs group. All results indicate that the FHMP NPs caused no detectable toxicity *in vivo*.

Furthermore, major organs of the mice, including the heart, liver, spleen, lung, and kidney, were collected and sectioned for H&E staining after the treatments to observe the corresponding pathological toxicity. It is clear that no adverse effect was found during the treatment period for all groups, suggesting no significant histological abnormality in the treatment group (**Figure 8D**). All these results suggest that the FHMP NPs are highly biocompatible and biodegradable *in vivo*.

Conclusions

In summary, we successfully constructed a PLGA-loaded multifunctional FA-targeted theranostic nanoplatform (FHMP NPs) for PA imaging-guided SDT of cancer cells/tissue. Such an intriguing contrast agent is highly useful in PA imaging for detecting tumors as well as for delineating tumor regions. Especially, upon exposure of FHMP NPs to US, a large quantity of ROS was generated based on the sonosensitizing effect of FHMP NPs. Both *in vitro* cell-level evaluation and *in vivo* tumor-xenograft experiments identified the FA ligand-mediated active targeting with high specificity to tumor cells, which achieved a large accumulation of FHMP NPs in the tumor region compared to that of nontargeted NPs. In addition, based on the ROS generation, the therapeutic effect on tumors was also evaluated and demonstrated for efficient tumor

ablation without obvious reoccurrence. Importantly, the integrated biocompatible components endowed this nanoplatform with excellent compatibility and biodegradability in the studied concentration range, which guarantee their further clinical translation. Therefore, this work not only reports a novel theranostic probe for tumor detection and treatment but also provides convincing evidence on supporting the highly targeted therapeutic efficacy of FHMP NPs under US irradiation.

Abbreviations

ALB: albumin; ALT: alanine transaminase; ALP: alkaline phosphatase; AST: aspartate transaminase; BUN: urea nitrogen; CHCl₃: chloroform; Calcein-AM: Calcein acetoxymethyl ester; CCK-8: Cell Counting Kit-8; CLSM: confocal laser scanning microscopy; DAPI: 4,6-diamidino-2-phenylindole; DCFH-DA: 2,7-dichlorodi-hydrofluoresceindiacetate; DiI: 1,1-dioctadecyl-3,3,3',3'-tetramethylindocarbocyanine perchlorate; DiR: 1,1'-dioctadecyl-3,3,3',3'-tetramethylindotricarbocyanine iodide; DPBF: 1,3-diphenylisobenzofuran; FA: folate; FBS: fetal bovine serum; FDA: Food and Drug Administration; FHP NPs: FA-HMME-PLGA NPs; FHMP NPs: FA-HMME-MNPs-PLGA NPs; HMME: hematoporphyrin monomethyl ether; FMP NPs: FA-MNPs-PLGA NPs; H&E: hematoxylin-eosin staining; HMP NPs: HMME-MNPs-PLGA NPs; LIFU: low-intensity focused ultrasound; MNPs: melanin NPs; NAC: N-acetyl-L-cysteine; OD: optical density; PA: photoacoustic; PBS: phosphate-buffered solution; PEG-MNP: pegylated polydopamine NPs; PEG-MNP-CA: pegylated polydopamine NPs decorated with citraconic amide; Gd-64 Cu-PEG-MNP: pegylated polydopamine NPs loaded with Gd³⁺ and 64 Cu²⁺; PLGA: poly (lactic-co-glycolic) acid; PLT: platelets; PI: propidium iodide; PVA: poly(vinyl alcohol); PCNA: proliferating cell nuclear antigen; RBC: red blood cells; ROS: reactive oxygen species; RPMI-1640: Roswell Park Memorial Institute-1640; SEM: scanning electron microscopy; SDT: sonodynamic therapy; Scr: serum creatinine; SOSG: singlet oxygen sensor green; TEM: transmission electron microscopy; TUNEL: TdT-mediated dUTP nick-end labeling; US: ultrasound; UV-vis ultraviolet spectrophotometer; WBC: white blood cells.

Supplementary Material

Supplementary figures.

<http://www.thno.org/v08p6178s1.pdf>

Acknowledgements

The authors are greatly thankful for the financial

support by the National Natural Science Foundation of the People's Republic of China (grant nos. 81771847, 31630026, 81630047, 81771845 and 81501444), Chongqing colleges and universities outstanding achievement transformation fund project (grant nos: KJZH17109) and Precision medicine special project of Chongqing science and technology committee (grant nos: cstc2016shms-ztxz130001).

Competing Interests

The authors have declared that no competing interest exists.

References

- Zhou Y, Hu Y, Sun W, Zhou B, Zhu J, Peng C, et al. Polyaniline-loaded gamma-polyglutamic acid nanogels as a platform for photoacoustic imaging-guided tumor photothermal therapy. *Nanoscale*. 2017; 9: 12746-54.
- Cai Y, Liang P, Tang Q, Yang X, Si W, Huang W, et al. Diketopyrrolopyrrole-triphenylamine organic nanoparticles as multifunctional reagents for photoacoustic imaging-guided photodynamic/photothermal synergistic tumor therapy. *ACS Nano*. 2017; 11: 1054-63.
- Qian X, Zheng Y, Chen Y. Micro/nanoparticle-augmented sonodynamic therapy (SDT): breaking the depth shallow of photoactivation. *Adv Mater*. 2016; 28: 8097-129.
- Zhu P, Chen Y, Shi J. Nanoenzyme-augmented cancer sonodynamic therapy by catalytic tumor oxygenation. *ACS Nano*. 2018; 12: 3780-95.
- Dai C, Zhang S, Liu Z, Wu R, Chen Y. Two-dimensional graphene augments nanosensitized sonocatalytic tumor eradication. *ACS Nano*. 2017; 11: 9467-80.
- Yan S, Lu M, Ding X, Chen F, He X, Xu C, et al. Hematoporphyrin monomethyl ether polymer contrast agent for ultrasound/photoacoustic dual-modality imaging-guided synergistic high intensity focused ultrasound (HIFU) therapy. *Sci Rep*. 2016; 6: 31833.
- Xu F, Zhao Y, Hu M, Zhang P, Kong N, Liu R, et al. Lanthanide-doped core-shell nanoparticles as a multimodality platform for imaging and photodynamic therapy. *Chem Commun*. 2018; 54: 9525-8.
- Pan X, Bai L, Wang H, Wu Q, Wang H, Liu S, et al. Metal-organic-framework-derived carbon nanostructure augmented sonodynamic cancer therapy. *Adv Mater*. 2018; 30: e1800180.
- Xu F, Hu M, Liu C, Choi SK. Yolk-structured multifunctional up-conversion nanoparticles for synergistic photodynamic-sonodynamic antibacterial resistance therapy. *Biomater Sci*. 2017; 5: 678-85.
- Kuroki M, Hachimine K, Abe H, Shibaguchi H, Kuroki M, Maekawa S, et al. Sonodynamic therapy of cancer using novel sonosensitizers. *Anticancer Res*. 2007; 27: 3673-7.
- McEwan C, Owen J, Stride E, Fowley C, Nesbitt H, Cochrane D, et al. Oxygen carrying microbubbles for enhanced sonodynamic therapy of hypoxic tumours. *J Controlled Release*. 2015; 203: 51-6.
- McEwan C, Kamila S, Owen J, Nesbitt H, Callan B, Borden M, et al. Combined sonodynamic and antimetabolite therapy for the improved treatment of pancreatic cancer using oxygen loaded microbubbles as a delivery vehicle. *Biomaterials*. 2016; 80: 20-32.
- Deepagan VG, You DG, Um W, Ko H, Kwon S, Choi KY, et al. Long-circulating Au-TiO₂ nanocomposite as a sonosensitizer for ROS-mediated eradication of cancer. *Nano Lett*. 2016; 16: 6257-64.
- Zhang K, Xu H, Jia X, Chen Y, Ma M, Sun L, et al. Ultrasound-triggered nitric oxide release platform based on energy transformation for targeted inhibition of pancreatic tumor. *ACS Nano*. 2016; 10: 10816-28.
- Chen J, Luo H, Liu Y, Zhang W, Li H, Luo T, et al. Oxygen-self-produced nanopatform for relieving hypoxia and breaking resistance to sonodynamic treatment of pancreatic cancer. *ACS Nano*. 2017; 11: 12849-62.
- Zhang K, Xu H, Chen H, Jia X, Zheng S, Cai X, et al. CO₂ bubbling-based 'nanobomb' system for targetedly suppressing panc-1 pancreatic tumor via low intensity ultrasound-activated inertial cavitation. *Theranostics*. 2015; 5: 1291-302.
- Zhang K, Chen H, Li F, Wang Q, Zheng S, Xu H, et al. A continuous tri-phase transition effect for HIFU-mediated intravenous drug delivery. *Biomaterials*. 2014; 35: 5875-85.
- Yu ll. Advance in the second generation of photosensitizer hematoporphyrin monomethyl ether and its clinical applications. *Biomed Eng Clin Med*. 2005; 9: 365-8.
- Zhang HK, Chen Y, Kang J, Lisok A, Minn I, Pomper MG, et al. Prostate-specific membrane antigen-targeted photoacoustic imaging of prostate cancer in vivo. *J Biophotonics*. 2018; e201800021.
- Jia Q, Ge J, Liu W, Liu S, Niu G, Guo L, et al. Gold nanorod@silica-carbon dots as multifunctional phototheranostics for fluorescence and photoacoustic imaging-guided synergistic photodynamic/photothermal therapy. *Nanoscale*. 2016; 8: 13067-77.
- Ao M, Wang Z, Ran H, Guo D, Yu J, Li A, et al. Gd-DTPA-loaded PLGA microbubbles as both ultrasound contrast agent and MRI contrast agent—a feasibility research. *J Biomed Mater Res*. 2010; 93: 551-6.
- Zhang R, Fan Q, Yang M, Cheng K, Lu X, Zhang L, et al. Engineering melanin nanoparticles as an efficient drug-delivery system for imaging-guided chemotherapy. *Adv Mater*. 2015; 27: 5063-9.
- Longo D L, Stefania R, Callari C, et al. Water soluble melanin derivatives for dynamic contrast enhanced photoacoustic imaging of tumor vasculature and response to antiangiogenic therapy. *Adv Health Mater*. 2017; 6.
- Fan Q, Cheng K, Hu X, et al. Transferring biomarker into molecular probe: melanin nanoparticle as a naturally active platform for multimodality imaging. *J Am Chem Soc*. 2014; 136: 15185-94.
- Zhang L, Sheng D, Wang D, et al. Bioinspired multifunctional melanin-based nanoliposome for photoacoustic/magnetic resonance imaging-guided efficient photothermal ablation of cancer. *Theranostics*. 2018; 8: 1591.
- Liopo A, Su R, Oraevsky AA. Melanin nanoparticles as a novel contrast agent for optoacoustic tomography. *Photoacoustics*. 2015; 3: 35-43.
- Ju KY, Kang J, Pyo J, Lim J, Chang JH, Lee JK. pH-Induced aggregated melanin nanoparticles for photoacoustic signal amplification. *Nanoscale*. 2016; 8: 14448-56.
- Shao J, Xie H, Huang H, Li Z, Sun Z, Xu Y, et al. Biodegradable black phosphorus-based nanospheres for in vivo photothermal cancer therapy. *Nat Commun*. 2016; 7: 12967.
- Petros RA, DeSimone JM. N. Strategies in the design of nanoparticles for therapeutic applications. *Nat Rev Drug Discovery*. 2010; 9: 615-27.
- Assaraf YG, Leamon CP, Reddy JA. The folate receptor as a rational therapeutic target for personalized cancer treatment. *Drug Resist Updates*. 2014; 17: 89-95.
- Trendowski M. The promise of sonodynamic therapy. *Cancer Metastasis Rev*. 2014; 33: 143-60.
- Sun Y, Zheng Y, Ran H, Zhou Y, Shen H, Chen Y, et al. Superparamagnetic PLGA-iron oxide microcapsules for dual-modality US/MR imaging and high intensity focused US breast cancer ablation. *Biomaterials*. 2012; 33: 5854-64.
- Augustine S, Singh J, Srivastava M, Sharma M, Das A, Malhotra BD. Recent advances in carbon based nanosystems for cancer theranostics. *Biomaterials Sci*. 2017; 5: 901-52.
- Brigger I, Dubernet C, Couvreur P. Nanoparticles in cancer therapy and diagnosis. *Adv Drug Delivery Rev*. 2012; 64: 24-36.
- Chen Q, Xu L, Liang C, Wang C, Peng R, Liu Z. Photothermal therapy with immune-adjuvant nanoparticles together with checkpoint blockade for effective cancer immunotherapy. *Nat Commun*. 2016; 7: 13193.
- Niu C, Wang Z, Lu G, Krupka TM, Sun Y, You Y, et al. Doxorubicin loaded superparamagnetic PLGA-iron oxide multifunctional microbubbles for dual-mode US/MR imaging and therapy of metastasis in lymph nodes. *Biomaterials*. 2013; 34: 2307-17.
- Deng L, Cai X, Sheng D, Yang Y, Strohm EM, Wang Z, et al. A laser-activated biocompatible theranostic nanoagent for targeted multimodal imaging and photothermal therapy. *Theranostics*. 2017; 7: 4410-23.
- Zhang K, Li P, Chen H, et al. Continuous cavitation designed for enhancing radiofrequency ablation via a special radiofrequency solidoid vaporization process. *ACS Nano*. 2016; 10: 2549-58.
- Budhian A, Siegel S J, Winey K I. Haloperidol-loaded PLGA nanoparticles: systematic study of particle size and drug content. *Int J Pharm*. 2007; 336: 367.
- Shi J, Chen Z, Wang B, Wang L, Lu T, Zhang Z. Reactive oxygen species-manipulated drug release from a smart envelope-type mesoporous titanium nanovehicle for tumor sonodynamic-chemotherapy. *ACS App Mater Interfaces*. 2015; 7: 28554-65.
- Chen J, Luo H, Liu Y, Zhang W, Li H, Luo T, et al. Oxygen-self-produced nanopatform for relieving hypoxia and breaking resistance to sonodynamic treatment of pancreatic cancer. *ACS Nano*. 2017; 11: 12849-62.
- Gollavelli G, Ling YC. Magnetic and fluorescent graphene for dual modal imaging and single light induced photothermal and photodynamic therapy of cancer cells. *Biomaterials*. 2014; 35: 4499-507.
- Murphy NP, Lampe KJ. Fabricating PLGA microparticles with high loads of the small molecule antioxidant N-acetylcysteine that rescue oligodendrocyte progenitor cells from oxidative stress. *Biotechnol Bioeng*. 2018; 115: 246-56.
- Chen Y, Tezcan O, Li D, Beztzinna N, Lou B, Etrych T. Overcoming multidrug resistance using folate receptor-targeted and pH-responsive polymeric nanogels containing covalently entrapped doxorubicin. *Nanoscale*. 2017; 9: 10404-19.
- Lv Y, Cao Y, Li P, Liu J, Chen H, Hu W, et al. Ultrasound-triggered destruction of folate-functionalized mesoporous silica nanoparticle-loaded microbubble for targeted tumor therapy. *Adv Healthcare Mater*. 2017; 6: 1700354.
- Xu Z, Hou M, Shi X, Gao YE, Xue P, Liu S, et al. Rapidly cell-penetrating and reductive milieu-responsive nanoaggregates assembled from an amphiphilic folate-campthecin prodrug for enhanced drug delivery and controlled release. *Biomaterials Sci*. 2017; 5: 444-54.
- Lin H, Gao S, Dai C, Chen Y, Shi J. A two-dimensional biodegradable niobium carbide (MXene) for photothermal tumor eradication in NIR-I and NIR-II biowindows. *J Am Chem Soc*. 2017; 139: 16235-47.
- Yang Q, Peng J, Xiao Y, Li W, Tan L, Xu X, et al. Porous Au@Pt nanoparticles: therapeutic platform for tumor chemo-photothermal co-therapy and

- alleviating doxorubicin-induced oxidative damage. *ACS App. Mater Interfaces*. 2018; 10: 150-64.
49. Shi J, Wang L, Zhang J, Ma R, Gao J, Liu Y, et al. A tumor-targeting near-infrared laser-triggered drug delivery system based on GO@Ag nanoparticles for chemo-photothermal therapy and X-ray imaging. *Biomaterials*. 2014; 35: 5847-61.
50. Manikandan M, Hasan N, Wu HF. Platinum nanoparticles for the photothermal treatment of Neuro 2A cancer cells. *Biomaterials*. 2013; 34: 5833-42.
51. Wang S, Huang P, Nie L, Xing R, Liu D, Wang Z, et al. Single continuous wave laser induced photodynamic/plasmonic photothermal therapy using photosensitizer-functionalized gold nanostars. *Adv Mater*. 2013; 25: 3055-61.
52. Cheng L, Liu J, Gu X, Gong H, Shi X, Liu T, et al. PEGylated WS(2) nanosheets as a multifunctional theranostic agent for in vivo dual-modal CT/photoacoustic imaging guided photothermal therapy. *Adv Mater*. 2014; 26: 1886-93.
53. Yin W, Yan L, Yu J, Tian G, Zhou L, Zheng X, et al. High-throughput synthesis of single-layer MoS₂ nanosheets as a near-infrared photothermal-triggered drug delivery for effective cancer therapy. *ACS Nano*. 2014; 8: 6922-33.
54. Chen D, Dougherty CA, Zhu K, Hong H. Theranostic applications of carbon nanomaterials in cancer: Focus on imaging and cargo delivery. *J Controlled Release*. 2015; 210: 230-45.
55. Li H, Song SI, Song GY, Kim I. Non-covalently functionalized carbon nanostructures for synthesizing carbon-based hybrid nanomaterials. *J Nanosci Nanotechnol*. 2014; 14: 1425-40.
56. Song X, Chen Q, Liu Z. Recent advances in the development of organic photothermal nano-agents. *Nano Res*. 2014; 8: 340-54.